

## EFFICIENT METHANOL DESORPTION IN SHEAR INSTABILITY

JORMA HARJU,<sup>1,2</sup> JAIME E. PINEDA,<sup>1</sup> ANTON I. VASYUNIN,<sup>1,3</sup> PAOLA CASELLI,<sup>1</sup>  
STELLA S.R. OFFNER,<sup>4</sup> ALYSSA A. GOODMAN,<sup>5</sup> MIKA JUVELA,<sup>2</sup> OLLI SIPILÄ,<sup>1</sup> ALEXANDRE FAURE,<sup>6,7</sup>  
ROMANE LE GAL,<sup>5</sup> PIERRE HILY-BLANT,<sup>6,7</sup> JOÃO ALVES,<sup>8</sup> LUCA BIZZOCCHI,<sup>1</sup> ANDREAS BURKERT,<sup>9,1</sup>  
HOPE CHEN,<sup>5</sup> RACHEL K. FRIESEN,<sup>10</sup> ROLF GÜSTEN,<sup>11</sup> PHILIP C. MYERS,<sup>5</sup> ANNA PUNANOVA,<sup>1,3</sup>  
CLAIRE RIST,<sup>6,7</sup> ERIK ROSOLOWSKY,<sup>12</sup> STEPHAN SCHLEMMER,<sup>13</sup> YANCY SHIRLEY,<sup>14</sup>  
SILVIA SPEZZANO,<sup>1</sup> CHARLOTTE VASTEL,<sup>15,16</sup> AND LAURENT WIESENFIELD<sup>6,7</sup>

<sup>1</sup>Max-Planck-Institut für extraterrestrische Physik, Gießenbachstraße 1, 85748 Garching, Germany

<sup>2</sup>Department of Physics, P.O. BOX 64, 00014 University of Helsinki, Finland

<sup>3</sup>Ural Federal University, 620002, 19 Mira street, Yekaterinburg, Russia

<sup>4</sup>Astronomy Department, University of Texas, Austin, TX 78712, USA

<sup>5</sup>Harvard-Smithsonian Center for Astrophysics, 60 Garden Street, Cambridge MA 02138, USA

<sup>6</sup>Université Grenoble Alpes, IPAG, F-38000 Grenoble, France

<sup>7</sup>CNRS, IPAG, F-38000 Grenoble, France

<sup>8</sup>University of Vienna, Türkenschanzstraße 17, A-1880 Vienna, Austria

<sup>9</sup>Universitäts-Sternwarte, Ludwig-Maximilians-Universität München, Scheinerstraße 1, 81679 München, Germany

<sup>10</sup>Dunlap Institute for Astronomy and Astrophysics, University of Toronto, 50 St. George Street, Toronto M5S 3H4, Ontario, Canada

<sup>11</sup>Max-Planck-Institut für Radioastronomie, Auf dem Hügel 69, 53121 Bonn, Germany

<sup>12</sup>Department of Physics, 4-181 CCIS, University of Alberta, Edmonton, AB T6G 2E1, Canada

<sup>13</sup>I. Physikalisches Institut, Universität zu Köln, Zùlpicher Straße 77, 50937 Köln, Germany

<sup>14</sup>Steward Observatory, University of Arizona, 933 North Cherry Avenue, Tucson, AZ 85721, USA

<sup>15</sup>Université de Toulouse, UPS-OMP, IRAP, Toulouse, France

<sup>16</sup>CNRS, IRAP, 9 Avenue du Colonel Roche, BP 44346, F-31028 Toulouse Cedex 4, France

### ABSTRACT

We present ALMA maps of the starless molecular cloud core Ophiuchus/H-MM1 in the lines of deuterated ammonia (ortho-NH<sub>2</sub>D), methanol (CH<sub>3</sub>OH), and sulphur monoxide (SO). While the dense core is outlined by NH<sub>2</sub>D emission, the CH<sub>3</sub>OH and SO distributions form a halo surrounding the core. Because methanol is formed on grain surfaces, its emission highlights regions where desorption from grains is particularly efficient. Methanol and sulphur monoxide are most abundant in a narrow zone that follows one side of the core. The region of the brightest emission has a wavy structure that rolls up at one end. This is the signature of Kelvin-Helmholtz instability occurring in sheared flows. We suggest that in this zone, methanol and sulphur are released as a result of grain-grain collisions induced by shear vorticity.

*Keywords:* astrochemistry — ISM: molecules — ISM: kinematics and dynamics —  
ISM: individual(Ophiuchus/H-MM1)

## 1. INTRODUCTION

Unexpectedly high abundances of gaseous methanol ( $\text{CH}_3\text{OH}$ ) have been found in the outer parts of cold starless cores (Bizzocchi et al. 2014; Vastel et al. 2014; Spezzano et al. 2016; Jiménez-Serra et al. 2016; Punanova et al. 2018). The fractional abundances ( $\sim 10^{-9}$  relative to  $\text{H}_2$ ) exceed the predictions from pure gas-phase chemical models by orders of magnitude (Garrod et al. 2006; Bacmann & Faure 2016). Methanol is believed to form almost exclusively on the surfaces of dust grains via hydrogenation of frozen carbon monoxide ( $\text{CO}$ ; Watanabe & Kouchi 2002; Geppert et al. 2006), and it is a common constituent of interstellar ices. To be detectable in the gas phase, methanol must be released from grains as a result of heating or some non-thermal mechanism. In cold, starless cores, non-thermal processes are required, and of these the so-called reactive desorption, desorption caused by exothermic surface reactions, is currently the strongest candidate (Garrod et al. 2006; Garrod et al. 2007; Vasyunin & Herbst 2013; Balucani et al. 2015; Jiménez-Serra et al. 2016; Vasyunin et al. 2017). The efficiency of desorption after the molecule formation is, however, uncertain, and it is given as a free parameter in chemistry models (Minissale et al. 2016; Chuang et al. 2018).

While reactive desorption provides a plausible explanation for observed methanol distributions, it should be noted that core boundaries, where methanol is usually found, are also subject to dynamical effects, such as accretion, velocity shears, and turbulence. Several cores show a sharp transition from supersonic to subsonic turbulence in a thin layer surrounding the core (Goodman et al. 1998; Pineda et al. 2010; Friesen et al. 2017; Auddy et al. 2019). In this region, the scaling relation between the velocity dispersion,  $\sigma_v$ , and the scale length  $l$ ,  $\sigma_v \propto l^a$ , seems to break (Goodman et al. 1998), suggesting that part of the turbulent energy of

the surrounding gas is dissipated, while at the same time the exterior turbulence compresses the core. Also gravitational accretion from the surrounding cloud and collisions between cores can lead to conversion of kinetic energy into heat. These effects can contribute to the evaporation of the ice coatings of dust grains. Finally, the chemical composition of the outer parts of dense cores can be affected by the external radiation field, especially in the vicinity of young massive stars, and when the core lies near the edge of a cloud. Radiation is the main source of heat at the core boundaries, and can also directly influence the chemistry during the diffuse contraction phase (e.g., Spezzano et al. 2016).

Here we present maps of a nearby prestellar core in the spectral lines of methanol, deuterated ammonia ( $\text{NH}_2\text{D}$ ), and sulphur monoxide ( $\text{SO}$ ), obtained using the Atacama Large (Sub)millimeter Array (ALMA). The spatial resolution of these observations is  $\sim 500$  au. We discuss the origin of gas-phase methanol based on the observed molecular distributions and the physical conditions of the emission regions. In addition to reactive desorption, we identify low-velocity grain-grain collisions induced by turbulent grain acceleration as a possible mechanism enhancing methanol abundance in the envelopes of prestellar cores. The present observations suggest that vorticity associated with shear instability is a particularly effective way of inducing grain-grain collisions that lead to the removal methanol from grains.

## 2. OBSERVATIONS

The target of the present observations is the nearby prestellar core Ophiuchus/H-MM1 located on the eastern side of the L1688 cloud (Johnstone et al. 2004; Parise et al. 2011; Harju et al. 2017). The dimensions of the kidney-shaped dense core are approximately  $60'' \times 90''$ . The target is prominent in the  $850 \mu\text{m}$  dust continuum maps of Ophiuchus with SCUBA-2 (Pattle et al. 2015), and in the  $\text{NH}_3$  map

of L1688 from the Greenbank Ammonia Survey (Friesen et al. 2017).

The present data were taken during the ALMA cycle 4 (project 2016.1.00035.S). Here we discuss the  $J_k = 2_k - 1_k$  rotational lines of  $\text{CH}_3\text{OH}$  at 96.7 GHz and the  $J_{K_a, K_c} = 1_{11}^s - 1_{01}^a$  rotation-inversion line of ortho- $\text{NH}_2\text{D}$  at 85.9 GHz, which were observed simultaneously with the 3 millimeter continuum in the ALMA Band 3. The 'continuum' spectral window included the  $J_N = 3_2 - 2_1$  rotation line of SO at 99.3 GHz. This line is unresolved because the channel width in this spectral cube is  $\sim 4.9$  MHz ( $\sim 1.5 \text{ km s}^{-1}$ ).

An area of  $50'' \times 80''$  covering the densest part of the H-MM1 core was imaged using the ALMA 12 m array (40 antennas) in one of its most compact configurations, and the ALMA Compact Array (ACA) with 10 7 m antennas. The total power (TP) antennas were not used. With the 12 m array, the mapping was carried out by a five-point mosaic, whereas with the 7 m array, a single point was measured. The data were calibrated and imaged using the CASA version 4.7.2. The angular resolution of the final images is  $4''$ , corresponding to 480 au (assuming a distance of 120 pc; Lombardi et al. 2008).

The integrated intensity maps of the ortho- $\text{NH}_2\text{D}$ ,  $\text{CH}_3\text{OH}$  and SO lines at 85.9, 96.7 and 99.3 GHz, respectively, are shown in Figures 1a, b and c. The fourth map, shown in panel d of this figure, is the  $\text{H}_2$  column density map derived from  $8 \mu\text{m}$  extinction. For this we have used the  $8 \mu\text{m}$  surface brightness map measured by the InfraRed Array Camera (IRAC) of the Spitzer Space Telescope, smoothed to a  $4''$  resolution (the original resolution is  $\sim 2''$ ). The method used for deriving the  $N(\text{H}_2)$  map is described in Appendix A. The 3 mm continuum is weak, and the map from the present ALMA observations misses extended emission. Consequently, only the emission peak in the center of the core is detected by ALMA. The 3 mm con-

tinuum map using only the ACA data is shown in Figure 1d, as a contour plot superposed on the  $N(\text{H}_2)$  image.

The  $\text{NH}_2\text{D}$  map resembles the  $\text{H}_2$  column density map shown in Figure 1d, and the far-infrared dust emission maps of the core, e.g., the  $850 \mu\text{m}$  SCUBA-2 map shown in Figure 5. The  $\text{CH}_3\text{OH}$  and SO distributions closely resemble each other, and they are almost complementary to the  $\text{NH}_2\text{D}$  distribution; methanol and sulphur monoxide follow the edges of the elongated core but are stronger on the left, concave side of the core (the eastern side in the sky) than elsewhere.

### 3. ANALYSIS OF THE LINE DATA

Four lines of the  $(2_k - 1_k)$  group of  $\text{CH}_3\text{OH}$  were included in the spectral window around 96.7 GHz. Three of them belong to the  $E$  symmetry species and one to the  $A$  species. The rotational temperatures,  $T_{\text{rot}}$ , and the column densities,  $N$ , of  $E$ -type methanol were derived adopting the procedure described by Nummelin et al. (2000), where no assumption about the optical thickness of the lines is made. The rotational temperatures are in the range  $T_{\text{rot}} \sim 8 - 11$  K. The peak value of the  $E$ -methanol column density is  $N(E - \text{CH}_3\text{OH}) \sim 1.5 \times 10^{14} \text{ cm}^{-2}$ . In the region with bright  $\text{CH}_3\text{OH}$  emission, bordering the eastern side of the core,  $N(E - \text{CH}_3\text{OH}) \geq 6 \times 10^{13} \text{ cm}^{-2}$ . The  $A$ -methanol column density,  $N(A - \text{CH}_3\text{OH})$ , was estimated using the single  $A$ -line in the spectrum, assuming that the rotational temperatures of the  $A$  and  $E$  symmetry species are the same. The  $A/E$  ratios in the bright region are in the range 1.2 – 1.5 (the high-temperature statistical limit is 1). This indicates that  $N(\text{CH}_3\text{OH}) \sim 2 \times N(E - \text{CH}_3\text{OH})$ .

The data set contains only one spectrally unresolved SO line,  $J_N = 3_2 - 2_1$ , at 99.3 GHz. Therefore, we only can derive the lower limit of the SO column density assuming optically thin emission. In this approximation, the upper

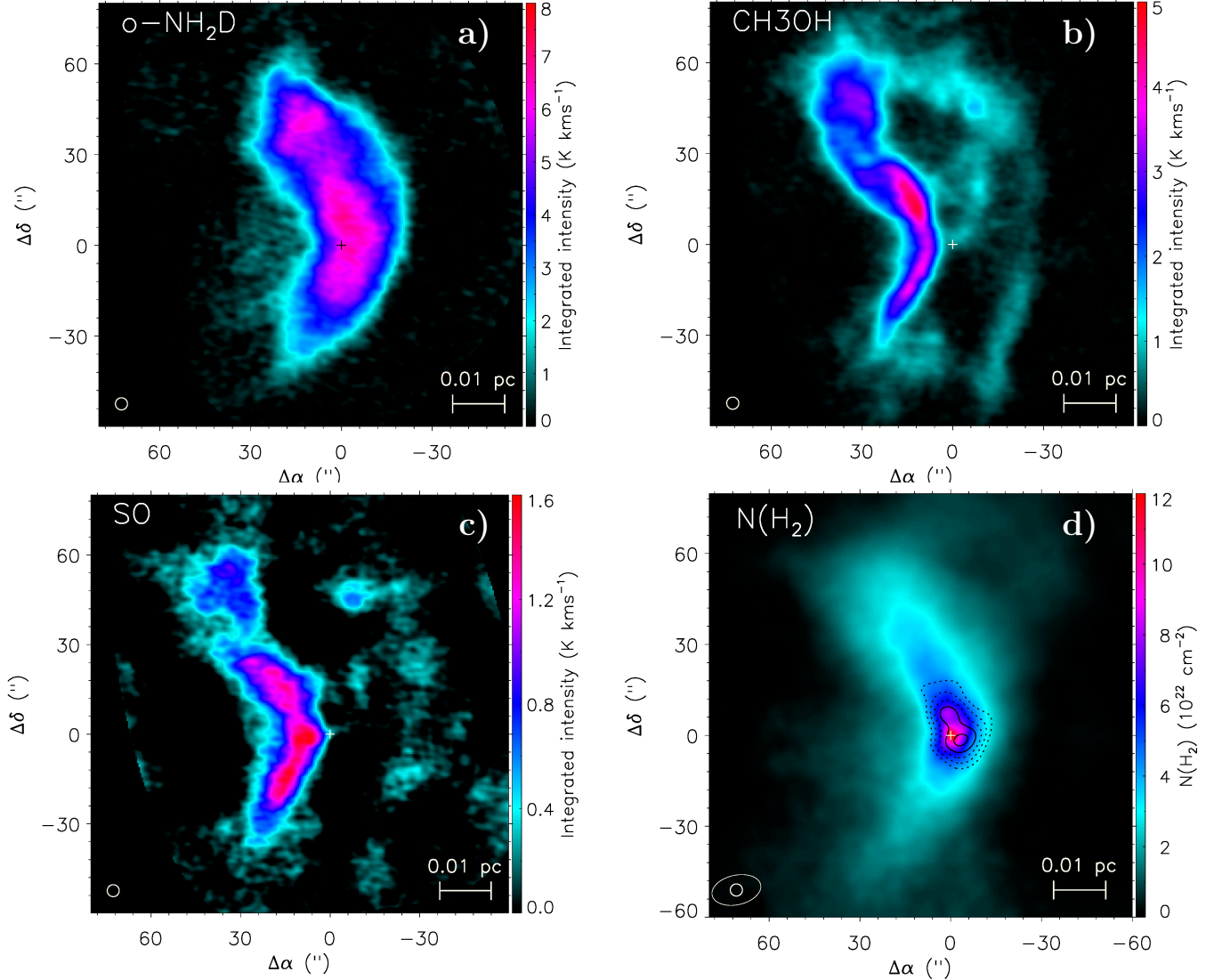


**Figure 1.** Molecular line maps and the  $\text{H}_2$  column density map of the core Ophiuchus/H-MM1. The panels (a), (b) and (c) show the integrated intensity maps of the ortho- $\text{NH}_2\text{D}(1_{11} - 1_{01})$ ,  $\text{CH}_3\text{OH}(2_k - 1_k)$  and  $\text{SO}(2_3 - 1_2)$  lines measured by ALMA. The synthetic beam size of the ALMA images ( $4''$ ) is indicated in the bottom left. The  $N(\text{H}_2)$  map of panel (d) is derived from  $8\mu\text{m}$  extinction, based on observations by the Spitzer Space Telescope. The contour lines show the 3 mm continuum emission measured by the ACA. The levels go from 2 to 3  $\text{mJy beam}^{-1}$  in steps of 0.25  $\text{mJy beam}^{-1}$ . The ellipse in the bottom left represents the synthetic beam of the ACA map. The plus sign indicates the position of the column density maximum with the coordinates RA 16:27:58.65, Dec. -24:33:41.2 (J2000).

state column density is directly proportional to the integrated brightness temperature,  $\int T_{\text{B}} dv$ , of the line. A rotation temperature, assumed to be the same for all rotational transitions, needs to be adopted for the calculation of the partition function. Assuming  $T_{\text{rot}} = 9\text{K}$ , we get  $N(\text{SO}) = 1.2 \times 10^{13} \text{ cm}^{-2} \times \int T_{\text{B}} dv$ , when the in-

tegral is in  $\text{K km s}^{-1}$ . For  $T_{\text{rot}} = 5\text{K}$ , the numerical factor before the integral is  $1.7 \times 10^{13} \text{ cm}^{-2}$ .

The fractional  $\text{CH}_3\text{OH}$  and  $\text{SO}$  abundance distributions were determined by dividing the column density maps by the  $N(\text{H}_2)$  map shown in Figure 1d. The fractional  $\text{CH}_3\text{OH}$  abundance map is shown in Figure 2. The estimates are limited to the region with bright

methanol emission, where the S/N ratio exceeds 3. The highest methanol abundances,  $X(\text{CH}_3\text{OH}) \sim 1 \times 10^{-8}$  (assuming equal abundances for the  $E$  and  $A$  types) are found at the eastern border of the core. The SO abundances are highest south of the methanol peak, with  $X(\text{SO}) \sim 5 - 8 \times 10^{-10}$ , depending on the assumed  $T_{\text{rot}}$  (9 or 5 K).

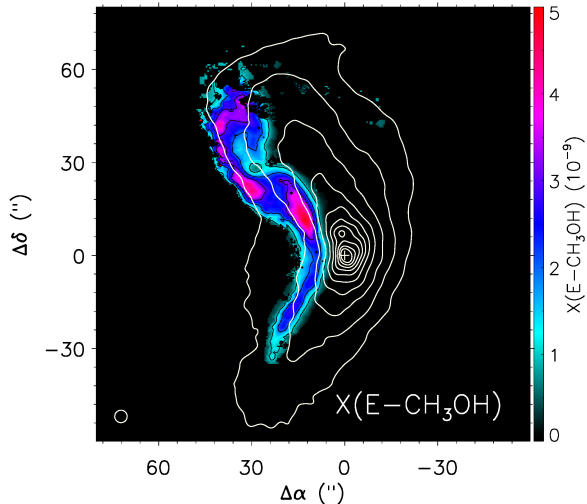


**Figure 2.** Fractional  $E - \text{CH}_3\text{OH}$  abundance distribution. The contours represent the  $\text{H}_2$  column density. They go from  $1 \times 10^{22} \text{ cm}^{-2}$  to  $10 \times 10^{22} \text{ cm}^{-2}$ .

In this paper, we only use the kinematic information from the  $\text{NH}_2\text{D}$  lines; the  $\text{NH}_2\text{D}$  column densities and fractional abundances will be discussed elsewhere. The ortho- $\text{NH}_2\text{D}$  spectral cube was analyzed by performing multicomponent Gaussian fits to the hyperfine structure of the  $1_{11} - 1_{01}$  line. The model used for the hyperfine structure takes into account the splittings owing to the electric quadrupole moments of both N and D nuclei (Daniel et al. 2016). The fits were made to positions where the signal-to-noise ratio exceeds 3. These fits give accurate estimates for the line velocity and width. The distributions of the one-dimensional velocity dispersion of the ortho- $\text{NH}_2\text{D}$  and  $\text{CH}_3\text{OH}$  lines are shown in Figure 3.

#### 4. DISCUSSION

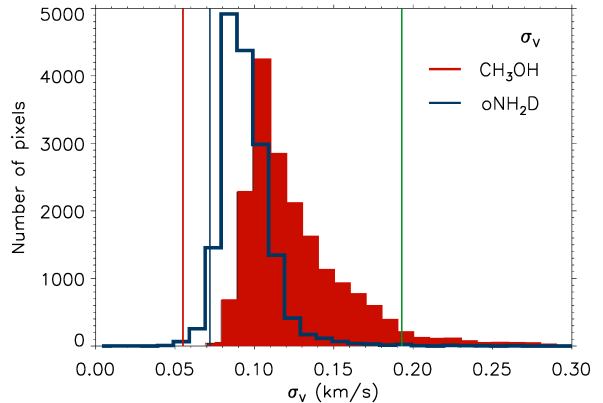


**Figure 3.** One-dimensional velocity dispersions of the ortho- $\text{NH}_2\text{D}$  and  $\text{CH}_3\text{OH}$  lines in Ophiuchus/H-MM1. These are obtained from Gaussian fits to the line profiles. The blue and red vertical lines indicate the thermal velocity dispersions of  $\text{NH}_2\text{D}$  and  $\text{CH}_3\text{OH}$  at 10 K. The green vertical line indicates the sound speed at this temperature. This Figure shows that methanol at the core interface has broader (non-thermal) line widths than  $\text{NH}_2\text{D}$ .

##### 4.1. Reactive desorption

In accordance with previous mappings, we find relatively high abundances of methanol in a prestellar core, offset from the density maximum. Thanks to the high spatial resolution achieved with ALMA, methanol emission in H-MM1 is found to be confined to a layer that follows the core boundaries. The projected thickness of this layer ranges from  $\sim 500$  au to  $\sim 1500$  au. The critical density of the co-existent  $\text{SO}(3_2 - 2_1)$  line is  $3 \times 10^5 \text{ cm}^{-3}$  at 10 K, whereas for the methanol lines this is  $3 \times 10^4 \text{ cm}^{-3}$ . We assume that the higher of these values,  $\sim 10^5 \text{ cm}^{-3}$ , is characteristic of the gas component detected in  $\text{CH}_3\text{OH}$  and  $\text{SO}$ . This value agrees with the densities derived by Bacmann & Faure (2016) for methanol emission regions in prestellar cores. At still higher densities, traced by  $\text{NH}_2\text{D}$ , both  $\text{CH}_3\text{OH}$  and  $\text{SO}$  are apparently frozen out. The behaviour of  $\text{CH}_3\text{OH}$  and  $\text{SO}$  conform, at least qualitatively, with the predictions of the reactive desorption model (Vasyunin et al. 2017; their Fig-

ures 4 and 8). In particular, the formation of methanol should be most efficient in the CO freeze-out zone at densities of  $10^4 - 10^5 \text{ cm}^3$ . This zone is characterized by the balance between CO depletion and the production of fresh CO in the gas phase. Reactive desorption is favored in this region by the fact that the surface of the icy mantles is dominated by the apolar, CO-rich component (Vasyunin et al. 2017). The reactive desorption model therefore naturally explains why  $\text{CH}_3\text{OH}$  seems to avoid the densest parts, and sometimes shows a shell-like distribution (Tafalla et al. 2006; Bizzocchi et al. 2014; Punanova et al. 2018).

Sulphur monoxide can form both in the gas phase and on grain surfaces. Without efficient desorption, gaseous SO depletes quickly at high densities. On the other hand, as soon as atomic sulphur is available in the gas phase, SO and other sulphur-bearing molecules are thought to form quickly in the gas phase through reactions with O,  $\text{O}_2$  and OH (Fuente et al. 2016; Vidal et al. 2017). Sulphur is probably released from ice mantles either as  $\text{H}_2\text{S}$  or in the atomic form. Methanol and sulphur monoxide are not directly related. Their spatial coincidence could possibly be explained by reactive codesorption of  $\text{CH}_3\text{OH}$  and SO or sulphur in some other form. Alternatively, gas-phase reactions forming SO may be efficient in the same conditions where  $\text{CH}_3\text{OH}$  is desorbed. In the model of Vasyunin et al. (2017), gaseous  $\text{CH}_3\text{OH}$  is abundant at a depth where water is partially photodissociated (their Figure 6). The presence of hydrogen atoms and hydroxyl radicals in this layer can also promote the formation of SO.

The strong asymmetry observed in H-MM1, and previously in the prestellar core L1544 (Spezzano et al. 2016; Punanova et al. 2018) is, however, difficult to explain without invoking an external agent. Spezzano et al. (2016) suggested that the methanol distribution in L1544 reflects asymmetric illumination which hinders

CO production on the more exposed side of the cloud. Intense radiation could also inhibit SO formation by keeping sulphur atoms ionized. The ionization energy of S is relatively low, 10.36 eV; the limiting wavelength of ionizing radiation,  $\lambda < 120 \text{ nm}$ , falls in the range where photons also can dissociate  $\text{CH}_3\text{OH}$  efficiently ( $114 \text{ nm} < \lambda < 180 \text{ nm}$ ; Cruz-Diaz et al. 2016).

The ambient cloud around H-MM1 continues towards the east, giving a reason to believe that the interstellar radiation field is indeed stronger on the side where  $\text{CH}_3\text{OH}$  and SO are weaker. This side faces the Upper Sco-Cen (USC) subgroup of the Scorpius-Centaurus OB association, including the luminous B-type double stars  $\rho$  Oph and HD 147889 (de Geus 1992; Preibisch & Mamajek 2008; Damiani et al. 2018). HD 147889, about 1.2 pc west of H-MM1, is the dominant UV source in the region (Liseau et al. 1999; Rawlings et al. 2013). The H-MM1 core is, however, embedded in the molecular cloud and the UV field at the core boundaries is probably weak. Methanol and SO emissions are confined within the column density contour  $N(\text{H}_2) = 10^{22} \text{ cm}^{-2}$ , which corresponds to a total visual extinction of  $A_V \sim 10^{\text{mag}}$  through the cloud. One can reasonably assume that the visual extinction from the cloud surface to the western edge of the core with weak  $\text{CH}_3\text{OH}$  emission is  $A_V \sim 5$  or higher. This implies that less than 0.2% of UV radiation with  $\lambda < 180 \text{ nm}$  will reach this region<sup>1</sup>, and that the scarcity of  $\text{CH}_3\text{OH}$  on the western side is not caused by photodissociation.

Nevertheless, dust grains are primarily heated by absorption of starlight, and the asymmetry in the radiation field can have caused a temperature difference between the two sides of the

<sup>1</sup> Estimated using the extinction law and formula from Cardelli et al. (1989), and assuming the extinction parameter value  $R_V = A_V/E_{B-V} = 4.0$  which is suggested to be appropriate for the  $\rho$  Ophiuchi cloud (Vrba et al. 1993; Whittet et al. 2001).

core, which in turn can influence on the abundances of CH<sub>3</sub>OH and SO. We examined this hypothesis using mid- to far-infrared maps from Spitzer, Herschel and SCUBA-2, and found that the dust temperature reaches its minimum on the eastern side of the core, close to the CH<sub>3</sub>OH maximum. The analysis of the dust continuum maps is presented in Appendix B.

The result of the analysis suggests that a temperature drop from about 14 – 15 K to about 11 – 12 K (see Fig. 5) favours methanol formation on grains. This is likely to be caused by effective accretion and hydrogenation of CO on grains at low temperatures. It should be noted, however, that the cooler region does not cover the whole eastern side of the core where strong CH<sub>3</sub>OH emission is found, and it does not extend to the SO maximum. At the northern and southern ends of the integral-shaped CH<sub>3</sub>OH and SO emission region, the dust temperature is similar to that on western side where these species show only weak emission.

#### 4.2. Shocks

Both CH<sub>3</sub>OH and SO are known to increase in shocks, and they have been used to probe outflows and the accretion process associated with star formation (Bachiller & Pérez Gutiérrez 1997; Podio et al. 2015; Oya et al. 2016). Strong enhancement of SO and SO<sub>2</sub> is predicted by models of magnetized molecular C-shocks, as a result of neutral-neutral reactions in the shock-heated gas and the erosion of S-rich icy grain mantles owing to bombardment by heated gas particles (Pineau des Forêts et al. 1993; Flower & Pineau des Forêts 1994). Sputtering of the grain mantles associated with shocks can also increase the CH<sub>3</sub>OH abundance substantially in the gas phase (Jiménez-Serra et al. 2008). Previous observations of mid-*J* CO rotational lines toward Perseus and Taurus complexes suggest low-velocity shocks associated with dissipation of turbulence and core formation in molecular clouds (Pon et al. 2014; Larson et al. 2015).

Judging from the fact that the non-thermal velocity dispersion experiences an abrupt change at the core boundary (Auddy et al. 2019; see Section 4.3), low-velocity shocks caused by accreting material are also possible in the case of H-MM1. However, the present data consisting of low-lying rotational lines CH<sub>3</sub>OH, SO, and NH<sub>2</sub>D do not show any evidence of shock heating or velocity gradients that would be large enough ( $\Delta v \gtrsim 10 \text{ km s}^{-1}$ ) to give rise to significant shock-induced sputtering.

#### 4.3. Grain-grain collisions in the turbulent envelope

The interior parts of the H-MM1 core have a very low level of non-thermal motions, as evinced by the velocity dispersion of the ortho-NH<sub>2</sub>D lines (Figure 3). In a study based on NH<sub>3</sub>(1, 1) and (2, 2) inversion line observations from the GreenBank Ammonia Survey (Friesen et al. 2017), Auddy et al. (2019) show that the non-thermal velocity dispersion increases suddenly at the boundaries of this and several other cores in Ophiuchus. Hydrodynamic drag and magnetic fields accelerate grains in a turbulent environment, and the acceleration is more effective for large grains than for small grains (Draine 1985; Lazarian & Yan 2002; Yan et al. 2004). This gives rise to velocity differences between small and large grains, and to an enhanced rate of grain-grain collisions.

As discussed by D’Hendecourt et al. (1982), low-velocity collisions between grains can lead to grain heating above the temperature threshold ( $\sim 30 \text{ K}$ ) that triggers explosive radical-radical reactions and the partial disruption of the grain mantle. Assuming that the grains consist of a silicate core and a mantle of water ice constituting  $\sim 15\%$  of the grain mass (corresponding to a fractional water abundance of  $\sim 10^{-4}$ ; van Dishoeck et al. 2013), one finds that the enthalpy change needed to raise the grain temperature from 10 K to 30 K corresponds to a collision velocity of  $\sim 30 \text{ m s}^{-1}$ . Here we have

used the Debye model for the heat capacity of the silicate core as a function of temperature (adopting the characteristics of olivine), and the formula from Shulman (2004) (their Eq. 4) for the heat capacity of water ice.

In Figure 4 we show relative grain velocities as a function of grain radius according to the models of Draine (1985) and Lazarian & Yan (2002), for conditions characteristic of the outer envelope of a cold dense core ( $T = 10$  K,  $n(\text{H}_2) = 10^5 \text{ cm}^{-3}$ ,  $B = 100 \mu\text{G}$ ). Here it is assumed that the turbulent velocity field has a Kolmogorov-like spectrum,  $v \propto l^{1/3}$ . The absolute scale is set by assuming that the turbulent velocity is  $0.8 \text{ km s}^{-1}$  on the scale  $0.05 \text{ pc}$ , which corresponds to the observed velocity gradient across the core ( $\Omega \sim v/l$ ; for discussion about the connection between velocity gradients and turbulence see Burkert & Bodenheimer 2000). Except for the smallest grains, the grain velocities are determined by turbulent velocity fluctuations occurring on a time scale comparable to that of the hydrodynamical drag. In Kolmogorov turbulence, the velocity is proportional to the square-root of the eddy turn-over time. Because the drag time is directly proportional to the grain radius,  $a$ , the velocity distribution of large grains has a square-root dependence on the grain radius,  $v \propto a^{1/2}$ . The smallest grains are also coupled to the magnetic field (a great majority of grains is negatively charged at visual extinctions above  $A_V \sim 3^{\text{mag}}$ ; Ivlev et al. 2015), and their velocity dispersion is determined by turbulent fluctuations on the time scale comparable to the Larmor time. This causes a  $v \propto a^{3/2}$  dependence for the smallest grains. Assuming the MRN grain size distribution (Mathis et al. 1977), the small, slow grains with velocities below  $10 \text{ m s}^{-1}$  comprise  $\sim 50\%$  of the total surface area of the grains, whereas the share of large, fast grains with  $v > 30 \text{ m s}^{-1}$  is only  $\sim 5\%$  of the surface area.

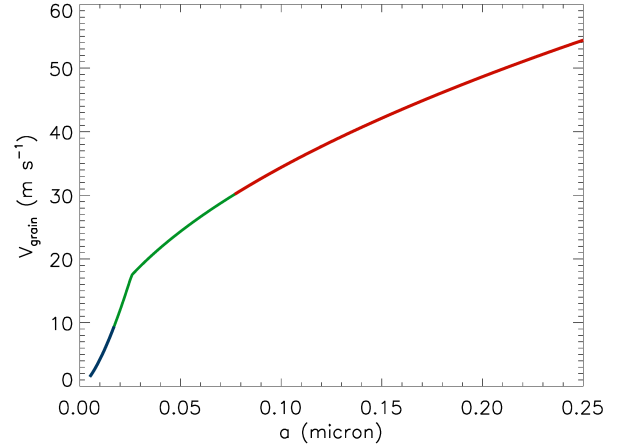


**Figure 4.** Relative speed of grains as a function of the grain radius according to the turbulent acceleration model (Draine 1985; Lazarian & Yan 2002) in dense dark cloud conditions (see text). The regimes of “high” and “low” velocity grains are indicated with red and blue, respectively. The discontinuity in the gradient is caused by the coupling of the smallest grains to the magnetic field.

Assuming that a given molecule X is being formed solely on the grains, and the number density of these molecules on the slow grains is  $n_X^{\text{surf,slow}}$  (corresponding in our example to  $\sim 50\%$  of the total number density,  $n_X^{\text{surf}}$ ), and that every collision between a slow and a fast grain leads to the complete desorption of molecules X from the surface of the small grain, the equilibrium gas-phase abundance of the molecule X,  $n_X^{\text{gas}}$ , can be written as

$$n_X^{\text{gas}} = \frac{n_X^{\text{surf,slow}} n_g^{\text{fast}} \pi (\bar{a}^{\text{fast}} + \bar{a}^{\text{slow}})^2 (\bar{v}_g^{\text{fast}} - \bar{v}_g^{\text{slow}})}{\Sigma_g \bar{v}_{\text{therm}}}, \quad (1)$$

where  $n_g^{\text{fast}}$  is the number density of fast grains,  $\bar{a}^{\text{fast}}$  and  $\bar{a}^{\text{slow}}$  are the average radii of the fast and slow grains, respectively,  $\bar{v}_g^{\text{fast}}$  and  $\bar{v}_g^{\text{slow}}$  are their average speeds,  $\Sigma_g$  is the total surface area of the grains per volume element, and  $\bar{v}_{\text{therm}}$  is the average thermal speed of the gas particles (D’Hendecourt et al. 1982; Caselli et al. 1997). The denominator is the depletion rate per molecule. When both particles are negatively charged, the kinetic energy overcomes the



Coulomb barrier in collisions between fast and slow grains.

The observed peak fractional abundance of methanol,  $\sim 1 \times 10^{-8}$  can be reproduced if the total methanol abundance on grains is  $n_{\text{CH}_3\text{OH}}^{\text{surf}}/n(\text{H}_2) \sim 5 \times 10^{-6}$ . The grain speeds decrease rapidly below the critical value ( $30 \text{ m s}^{-1}$ ) toward higher densities. On the other hand, at lower densities, the formation of methanol is inhibited because CO does not freeze onto grains efficiently enough. So, like in reactive desorption, the abundance of gaseous methanol owing to grain-grain collisions should peak at densities characteristic of core boundaries. The process should affect all atoms and molecules residing in the CO-rich outer layers of grain mantles, and this would explain why  $\text{CH}_3\text{OH}$  and SO have similar distributions.

In this scenario, the asymmetric distributions of  $\text{CH}_3\text{OH}$  and SO around H-MM1 would either indicate that turbulence is stronger on the eastern side of the core or that dust grain surfaces are richer in CO on that side. The latter suggestion is supported by the fact that the  $\text{CH}_3\text{OH}$  peak coincides with the dust temperature minimum (Appendix B). The former condition cannot be properly tested using the present data because the boundaries are not probed with any other lines than methanol and SO; the  $\text{NH}_2\text{D}$  line emission is confined to the inner regions where the lines are narrow. The angular resolution of the GreenBank  $\text{NH}_3$  maps ( $32''$ ; Friesen et al. 2017), which cover both the core and the ambient cloud, is not sufficient for detailed comparison of the velocity dispersions at the eastern and western boundaries. Nevertheless, a similar analysis as performed by Auddy et al. (2019), but averaging over semicircles, shows that the non-thermal velocity dispersion (measured along the line of sight) grows more slowly on the eastern side than on the western side, contradicting the supposition of a more vigorous

turbulence on that side. A diagram illustrating this difference is shown in Figure 6.

#### 4.4. Grain-grain collisions in a shear layer

One remarkable feature of the brightest  $\text{CH}_3\text{OH}$  emission region is that it closely follows the eastern boundary of the core as marked by  $\text{NH}_2\text{D}$  emission. The wavy shape and the rolling up seen in the north (Figure 2) are the hallmarks of Kelvin-Helmholtz instability (KHI), which can occur in sheared flows with density stratification. The methanol distribution gives the impression that the more tenuous gas at the eastern boundary flows to the north, more or less in the plane of the sky, or that the denser material of the core flows to the south. The presence of shear in a gas flow with a high Reynolds number implies small-scale vorticity, and the undulating methanol emission region probably consists of a chain of secondary billows that are unresolved in the present map. As described in standard textbooks, such as Batchelor (1967), advection of vorticity amplifies the dominant sinusoidal disturbance in a vortex sheet and makes it roll up. The evolution of vortex sheets has been studied numerically and semi-analytically by Patnaik et al. (1976) and Corcos & Sherman (1976). According to their results, vorticity reaches its maximum values at places they call “braids” (near the troughs) and “cores” or cat’s eyes (near the crests), separated by approximately half the wavelength of the dominant disturbance. By comparing the methanol map to the computed images of Patnaik et al. (1976), one can identify the methanol peak with a braid and the overturning billow in the north with a core. The apparent wavelength of the methanol feature is approximately  $60''$ , corresponding to  $7,200 \text{ au}$  or  $0.035 \text{ pc}$ .

In what follows, we attempt to estimate the flow properties, assuming that, in analogy with atmospheric billow clouds, the largest wavelength correspond to the so called internal gravity waves, which oscillate at the Brunt-Väisälä

frequency. This frequency, also known as the buoyancy frequency, is defined by  $N = \sqrt{\frac{-g}{\rho} \frac{\partial \rho}{\partial z}}$ , where  $g$  is the gravitational acceleration (directed to the negative  $z$  direction) and  $\rho$  is the gas density. We estimated the density and the density gradient in the supposed shear layer by fitting a Plummer-type function to the column density profile from the IRAC  $8 \mu\text{m}$  absorption. The method is explained by [Arzoumanian et al. \(2011\)](#).

The fit was made to the cross-sectional profile along an axis going through the methanol peak at RA 16:27:59.5, Dec. -24:33:30 (J2000). The axis is tilted with respect to the R.A. axis by  $25^\circ$ . According to this fit, the number densities at methanol peak and at the spine of cloud are  $\sim 4 \times 10^5 \text{ cm}^{-3}$  and  $\sim 1 \times 10^6 \text{ cm}^{-3}$ , respectively. The separation between these points is approximately  $10''$  (1,200 au). We assumed that the gravitational field at the methanol peak is dominated by the mass contained in a circular region of a radius of  $10''$ , centered at the crossing of the cloud spine and the cross-sectional axis. This mass is  $0.08 M_\odot$ . The Brunt-Väisälä frequency obtained is  $N \sim 1.4 \times 10^{-12} \text{ Hz}$  (period 140,000 yr). The multiplication  $N$  by the apparent wavelength gives a phase velocity of  $\sim 240 \text{ m s}^{-1}$ . This should correspond to the average speed of the sheared flow.

The fact that the flow is subject to KHI imposes a condition to the velocity shear: the Richardson number, defined by  $\text{Ri} = \frac{N^2}{(\partial v / \partial z)^2}$ , is less than  $1/4$ . The implied minimum shear is  $\sim 2.8 \times 10^{-12} \text{ s}^{-1}$  or  $\sim 90 \text{ km s}^{-1} \text{ pc}^{-1}$ . This value exceeds the north-south velocity gradient derived from the molecular line maps by a factor of 4-5. Assuming that the velocity at the outer boundary of the shear layer does not exceed  $400 \text{ m s}^{-1}$ , which is the typical non-thermal velocity far from the core, the maximum thickness of the layer is approximately 1000 au. This estimate agrees with the thickness of the methanol layer.

We conjecture that vorticity in the shear layer can accelerate dust grains to velocities deviating from the mean flow, and induce grain-grain collisions, in the same manner as Kolmogorov-type turbulence discussed in the previous section. However, the energy spectrum in a vortex sheet differs from that in fully developed turbulence which has  $E(k) \propto k^{-5/3}$ , where  $k$  is the wave number, and  $\int_0^\infty E(k) dk$  is the average kinetic energy per unit mass. Kraichnan suggested that, because of the conservation of the mean-square vorticity for two-dimensional turbulence in an inviscid fluid, the energy spectrum at the smallest scales should have the form  $E(k) \propto k^{-3} \{\ln(k/k_1)\}^{-1/3}$  for  $k \gg k_1$ , where  $k_1$  is the wavenumber at which vorticity is pumped in ([Kraichnan 1967](#); [Kraichnan 1971](#)). Numerical studies of two-dimensional turbulence give  $E(k) \propto k^{-\gamma}$ , where  $3 < \gamma < 4$  (e.g., [Gilbert 1988](#); [Abid & Verga 2011](#)). These energy spectra correspond to steeper velocity scaling laws than the Kolmogorov spectrum; the exponent  $\gamma = 3$  gives  $v \propto l$ , and  $\gamma = 4$  is equivalent to  $v \propto l^{3/2}$ .

The scaling law  $v \propto l$  implies one single time-scale in the energy cascade. Following the argumentation of [Draine \(1985\)](#), this would mean that grains with the drag time (corresponding to certain radius  $a$ ) comparable to this time-scale can be accelerated to any velocities present in the vortex sheet. Smaller grains would be advected by the swirling flow, whereas larger grains would not respond to the velocity fluctuations. The maximum speed is likely to be comparable with the free-stream velocity, estimated above to be of the order of  $200 \text{ m s}^{-1}$ . The time-scale depends on the structure of the vortex sheet. For a regular structure, such as the one given by the stream function in Eq. (3.9) of [Corcos & Sherman \(1976\)](#), the time-scale is  $\sim \lambda/U$ , where  $\lambda$  is the vortex size and  $U$  is the free-stream velocity. The maximum drag time for grains in the MRN size distribution is

$\sim 2,000$  yr in conditions described here. Using the speed mentioned above, we get for the vortex size  $\lambda < 80$  au.

Kraichnan’s energy spectrum with the logarithmic correction and any simple power law with  $\gamma > 3$  would imply that the smallest grains are accelerated to the highest speeds. For example, the formula of Kraichnan (1971) gives approximately  $v \propto a^{-1}$ , and the power  $\gamma = 4$  gives  $v \propto a^{-3}$ .

In view of the uncertainties concerning the “vertical” scale and the structure of the vorticity, we do not attempt to estimate methanol production rate in the suggested vortex sheet. We merely state that the present observations indicate that the formation methanol is more efficient in this layer than elsewhere in the core envelope. We suggest, based on the theoretical and numerical studies quoted above, that this is caused by the fact that two-dimensional turbulence can have larger velocity fluctuations than full three-dimensional turbulence on a time scale comparable to the drag time of dust grains.

## 5. CONCLUSIONS

Gaseous methanol and sulphur monoxide co-exist on the outskirts of the prestellar core H-MM1 in Ophiuchus. They are confined to a halo which follows the core boundaries and which is particularly prominent on the eastern side of the core. Because methanol is mainly produced on grains, the emission indicates regions of enhanced desorption. Sulphur monoxide may have co-desorbed with  $\text{CH}_3\text{OH}$  or formed in the gas phase following the release of  $\text{H}_2\text{S}$ .

We suggest that in addition to desorption caused by spontaneous exothermic surface reactions (Vasyunin et al. 2017), also grain-grain collisions can efficiently release molecules from grains in the core envelope. The latter mechanism is likely to proceed through mild heating that triggers explosive radical-radical reactions and partial disruption of grain mantles (D’Hendecourt et al. 1982). Collisions between

grains can be induced by Kolmogorov turbulence (Draine 1985; Lazarian & Yan 2002), or by shear vorticity.

The brightest methanol emission region at the eastern boundary of the core shows signatures of Kelvin-Helmholtz instability, indicating strong velocity shear. On the other hand, the non-thermal velocity dispersion along the line of sight, as traced by  $\text{NH}_3$  lines, grows more steeply on the opposite side of the core, where both  $\text{CH}_3\text{OH}$  and  $\text{SO}$  emissions are weak. We interpret this so that at the eastern boundary, laminar flow occurring in the plane of the sky is currently transitioning into turbulence through shear instability, whereas on the western side, the flow has already developed into full three-dimensional turbulence. The asymmetries of the  $\text{CH}_3\text{OH}$  and  $\text{SO}$  distributions suggest that shear vorticity induces more energetic or more frequent grain-grain collisions than Kolmogorov turbulence. This is likely to be related to the fact that two-dimensional turbulence has steeper energy spectrum (Kraichnan 1971), implying larger velocity fluctuations on the time scale needed to accelerate grains through hydrodynamic drag.

We thank Tom Hartquist, David Williams, Kalevi Mattila, and Hannu Savijärvi for helpful and enjoyable conversations. This paper makes use of the following ALMA data: ADS/JAO.ALMA#2016.1.00035.S. ALMA is a partnership of ESO (representing its member states), NSF (USA) and NINS (Japan), together with NRC (Canada), MOST and ASIAA (Taiwan), and KASI (Republic of Korea), in cooperation with the Republic of Chile. The Joint ALMA Observatory is operated by ESO, AUI/NRAO and NAOJ. The National Radio Astronomy Observatory is a facility of the National Science Foundation operated under cooperative agreement by Associated Universities, Inc.

This work is based in part on observations made with the Spitzer Space Telescope, and made use of the NASA/IPAC Infrared Science Archive. These facilities are operated by the Jet Propulsion Laboratory, California Institute

of Technology under a contract with National Aeronautics and Space Administration. This work was supported by the Academy of Finland (grants 285769 and 307157).

## REFERENCES

- Abid, M., & Verga, A. 2011, *PhRvE*, 84, 026318
- Arzoumanian, D., André, P., Didelon, P., et al. 2011, *A&A*, 529, L6
- Auddy, S., Myers, P. C., Basu, S., et al. 2019, *ApJ*, 872, 207
- Bachiller, R., & Pérez Gutiérrez, M. 1997, *ApJL*, 487, L93
- Bacmann, A., & Faure, A. 2016, *A&A*, 587, A130
- Balucani, N., Ceccarelli, C., & Taquet, V. 2015, *MNRAS*, 449, L16
- Batchelor, G. K. 1967, 1, Vol. 1, *An introduction to Fluid Dynamics*, 1st edn. (Cambridge: Cambridge University Press), ch. 7
- Bizzocchi, L., Caselli, P., Spezzano, S., & Leonardo, E. 2014, *A&A*, 569, A27
- Burkert, A., & Bodenheimer, P. 2000, *ApJ*, 543, 822
- Butler, M. J., & Tan, J. C. 2009, *ApJ*, 696, 484
- Cardelli, J. A., Clayton, G. C., & Mathis, J. S. 1989, *ApJ*, 345, 245
- Caselli, P., Hartquist, T. W., & Havnes, O. 1997, *A&A*, 322, 296
- Chuang, K.-J., Fedoseev, G., Qasim, D., et al. 2018, *ApJ*, 853, 102
- Corcos, G. M., & Sherman, F. S. 1976, *Journal of Fluid Mechanics*, 73, 241
- Cruz-Díaz, G. A., Martín-Doménech, R., Muñoz Caro, G. M., & Chen, Y.-J. 2016, *A&A*, 592, A68
- Damiani, F., Prisinzano, L., Pillitteri, I., Micela, G., & Sciortino, S. 2018, *ArXiv* 1807.11884, arXiv:1807.11884
- Daniel, F., Coudert, L. H., Punanova, A., et al. 2016, *A&A*, 586, L4
- de Geus, E. J. 1992, *A&A*, 262, 258
- D’Hendecourt, L. B., Allamandola, L. J., Baas, F., & Greenberg, J. M. 1982, *A&A*, 109, L12
- Draine, B. T. 1985, in *Protostars and Planets II*, ed. D. C. Black & M. S. Matthews, 621–640
- Flower, D. R., & Pineau des Forets, G. 1994, *MNRAS*, 268, 724
- Friesen, R. K., Pineda, J. E., co-PIs, et al. 2017, *ApJ*, 843, 63
- Fuente, A., Cernicharo, J., Roueff, E., et al. 2016, *A&A*, 593, A94
- Garrod, R., Park, I. H., Caselli, P., & Herbst, E. 2006, *Faraday Discussions*, 133, 51
- Garrod, R. T., Wakelam, V., & Herbst, E. 2007, *A&A*, 467, 1103
- Geppert, W. D., Hamberg, M., Thomas, R. D., et al. 2006, *Faraday Discussions*, 133, 177
- Gilbert, A. D. 1988, *Journal of Fluid Mechanics*, 193, 475
- Goodman, A. A., Barranco, J. A., Wilner, D. J., & Heyer, M. H. 1998, *ApJ*, 504, 223
- Harju, J., Daniel, F., Sipilä, O., et al. 2017, *A&A*, 600, A61
- Ho, P. T. P., & Townes, C. H. 1983, *ARA&A*, 21, 239
- Ivlev, A. V., Padovani, M., Galli, D., & Caselli, P. 2015, *ApJ*, 812, 135
- Jiménez-Serra, I., Caselli, P., Martín-Pintado, J., & Hartquist, T. W. 2008, *A&A*, 482, 549
- Jiménez-Serra, I., Vasyunin, A. I., Caselli, P., et al. 2016, *ApJL*, 830, L6
- Johnstone, D., Di Francesco, J., & Kirk, H. 2004, *ApJL*, 611, L45
- Juvela, M. 2019, *A&A*, 622, A79
- Kraichnan, R. H. 1967, *Physics of Fluids*, 10, 1417
- . 1971, *Journal of Fluid Mechanics*, 47, 525
- Larson, R. L., Evans, II, N. J., Green, J. D., & Yang, Y.-L. 2015, *ApJ*, 806, 70
- Lazarian, A., & Yan, H. 2002, *ApJL*, 566, L105
- Liseau, R., White, G. J., Larsson, B., et al. 1999, *A&A*, 344, 342
- Lombardi, M., Lada, C. J., & Alves, J. 2008, *A&A*, 480, 785
- Mathis, J. S., Ruml, W., & Nordsieck, K. H. 1977, *ApJ*, 217, 425
- Minissale, M., Dulieu, F., Cazaux, S., & Hocuk, S. 2016, *A&A*, 585, A24

- Nummelin, A., Bergman, P., Hjalmarson, Å., et al. 2000, *ApJS*, 128, 213
- Ossenkopf, V., & Henning, T. 1994, *A&A*, 291, 943
- Oya, Y., Sakai, N., López-Sepulcre, A., et al. 2016, *ApJ*, 824, 88
- Parise, B., Belloche, A., Du, F., Güsten, R., & Menten, K. M. 2011, *A&A*, 526, A31
- Patnaik, P. C., Sherman, F. S., & Corcos, G. M. 1976, *Journal of Fluid Mechanics*, 73, 215
- Pattle, K., Ward-Thompson, D., Kirk, J. M., et al. 2015, *MNRAS*, 450, 1094
- Pineau des Forêts, G., Roueff, E., Schilke, P., & Flower, D. R. 1993, *MNRAS*, 262, 915
- Pineda, J. E., Goodman, A. A., Arce, H. G., et al. 2010, *ApJL*, 712, L116
- Podio, L., Codella, C., Gueth, F., et al. 2015, *A&A*, 581, A85
- Pon, A., Johnstone, D., Kaufman, M. J., Caselli, P., & Plume, R. 2014, *MNRAS*, 445, 1508
- Preibisch, T., & Mamajek, E. 2008, *The Nearest OB Association: Scorpius-Centaurus (Sco OB2)*, ed. B. Reipurth, 235
- Punanova, A., Caselli, P., Feng, S., et al. 2018, *ApJ*, 855, 112
- Rawlings, M. G., Juvela, M., Lehtinen, K., Mattila, K., & Lemke, D. 2013, *MNRAS*, 428, 2617
- Shulman, L. M. 2004, *A&A*, 416, 187
- Spezzano, S., Bizzocchi, L., Caselli, P., Harju, J., & Brünken, S. 2016, *A&A*, 592, L11
- Tafalla, M., Santiago-García, J., Myers, P. C., et al. 2006, *A&A*, 455, 577
- van Dishoeck, E. F., Herbst, E., & Neufeld, D. A. 2013, *Chemical Reviews*, 113, 9043
- Vastel, C., Ceccarelli, C., Lefloch, B., & Bachiller, R. 2014, *ApJL*, 795, L2
- Vasyunin, A. I., Caselli, P., Dulieu, F., & Jiménez-Serra, I. 2017, *ApJ*, 842, 33
- Vasyunin, A. I., & Herbst, E. 2013, *ApJ*, 769, 34
- Vidal, T. H. G., Loison, J.-C., Jaziri, A. Y., et al. 2017, *MNRAS*, 469, 435
- Vrba, F. J., Coyne, G. V., & Tapia, S. 1993, *AJ*, 105, 1010
- Watanabe, N., & Kouchi, A. 2002, *ApJL*, 571, L173
- Whittet, D. C. B., Gerakines, P. A., Hough, J. H., & Shenoy, S. S. 2001, *ApJ*, 547, 872
- Yan, H., Lazarian, A., & Draine, B. T. 2004, *ApJ*, 616, 895

## APPENDIX

A. COLUMN DENSITY MAP FROM  $8\ \mu\text{m}$  EXTINCTION

The core is obscured from ultraviolet radiation and it serves as an absorbing component at  $8\ \mu\text{m}$ . The surface brightness in the core region can therefore be written as  $I^{8\ \mu\text{m}} = I_{\text{bg}}^{8\ \mu\text{m}} e^{-\tau^{8\ \mu\text{m}}} + I_{\text{fg}}^{8\ \mu\text{m}}$ , where  $\tau^{8\ \mu\text{m}}$  is the optical thickness at  $8\ \mu\text{m}$ ,  $I_{\text{bg}}$  is the surface brightness at the background of the core, and  $I_{\text{fg}}$  is the surface brightness of the foreground component (see, e.g., [Butler & Tan 2009](#)). The latter term may also contain a zero point offset. The optical thickness map can be obtained from

$$\tau^{8\ \mu\text{m}} = -\ln \left\{ \frac{I^{8\ \mu\text{m}} - I_{\text{fg}}^{8\ \mu\text{m}}}{I_{\text{bg}}^{8\ \mu\text{m}}} \right\}.$$

In order to estimate the background emission,  $I_{\text{bg}}^{8\ \mu\text{m}}$ , we made a fit to the surface brightness distribution with the core masked out. For masking we used the SCUBA-2  $850\ \mu\text{m}$  map. The foreground component,  $I_{\text{fg}}^{8\ \mu\text{m}}$  (including possible zero-point offset), was assumed to be constant in the mapped region. Its value was estimated by requiring that the ratio of the peak optical thicknesses is  $\tau^{8\ \mu\text{m}}/\tau^{850\ \mu\text{m}} = 780$ , corresponding to the adopted dust opacity model, which was the model for unprocessed dust grains with thin ice mantles by [Ossenkopf & Henning \(1994\)](#). The comparison was done using an IRAC map smoothed to the resolutions of the SCUBA map.

At  $850\ \mu\text{m}$ , the core is optically thin and it is seen in thermal dust emission. The observing method filters out extended emission. The surface brightness is therefore  $I^{850\ \mu\text{m}} = B^{850\ \mu\text{m}}(T_{\text{d}}) \tau^{850\ \mu\text{m}}$ , where  $T_{\text{d}}$  is the dust temperature and  $B$  is the Planck function. The opacity map at  $850\ \mu\text{m}$ ,  $\tau^{850\ \mu\text{m}}$ , was calculated by combining the  $850\ \mu\text{m}$  surface brightness map with the dust color temperature map,  $T_{\text{C}}$ , derived from Herschel/SPIRE maps ([Harju et al. 2017](#)). The angular resolution of the  $T_{\text{C}}$  map is  $\sim 40''$ , whereas for SCUBA it is approximately  $14''$ . We think this discrepancy in the angular resolutions is acceptable because the  $850\ \mu\text{m}$  surface brightness is not very sensitive to the dust temperature (see below).

Finally,  $\text{H}_2$  column density map shown in Fig. 1d) was calculated by dividing the  $8\ \mu\text{m}$  optical thickness map by the absorption cross-section of dust per  $\text{H}_2$  molecule, which according to the adopted dust model is  $4.1 \times 10^{-23}\ \text{cm}^2\ \text{H}_2\ \text{molecule}^{-1}$  ( $8.86\ \text{cm}^2\ \text{g}^{-1}$ ).

## B. DUST TEMPERATURE DISTRIBUTION

At  $70\ \mu\text{m}$ , a cloud can be seen either in absorption or emission depending on the dust temperature and the brightness of the background. At this wavelength, the Planck function is very sensitive to small changes in the temperature. For example, a temperature change from 12 to 14 K for a given dust column increases the emission by an order of magnitude, while at  $850\ \mu\text{m}$ , the corresponding change is  $\sim 20\%$ . The surface brightness at  $70\ \mu\text{m}$  takes the form

$$I^{70\ \mu\text{m}} = I_{\text{bg}}^{70\ \mu\text{m}} e^{-\tau^{70\ \mu\text{m}}} + I_{\text{fg}}^{70\ \mu\text{m}} + B^{70\ \mu\text{m}}(T_{\text{d}})(1 - e^{-\tau^{70\ \mu\text{m}}}).$$

We assumed that the  $\tau^{70\ \mu\text{m}}$  distribution is identical to that at  $8\ \mu\text{m}$  save a constant factor depending on the adopted dust opacity model (giving  $\tau^{8\ \mu\text{m}}/\tau^{70\ \mu\text{m}} = 1.2$ ). The foreground level (including a possible zero-point offset) was adjusted so that the dust temperatures on the outskirts of the core are similar to  $T_{\text{C}}$  values derived from Herschel/SPIRE. The obtained dust temperature distribution

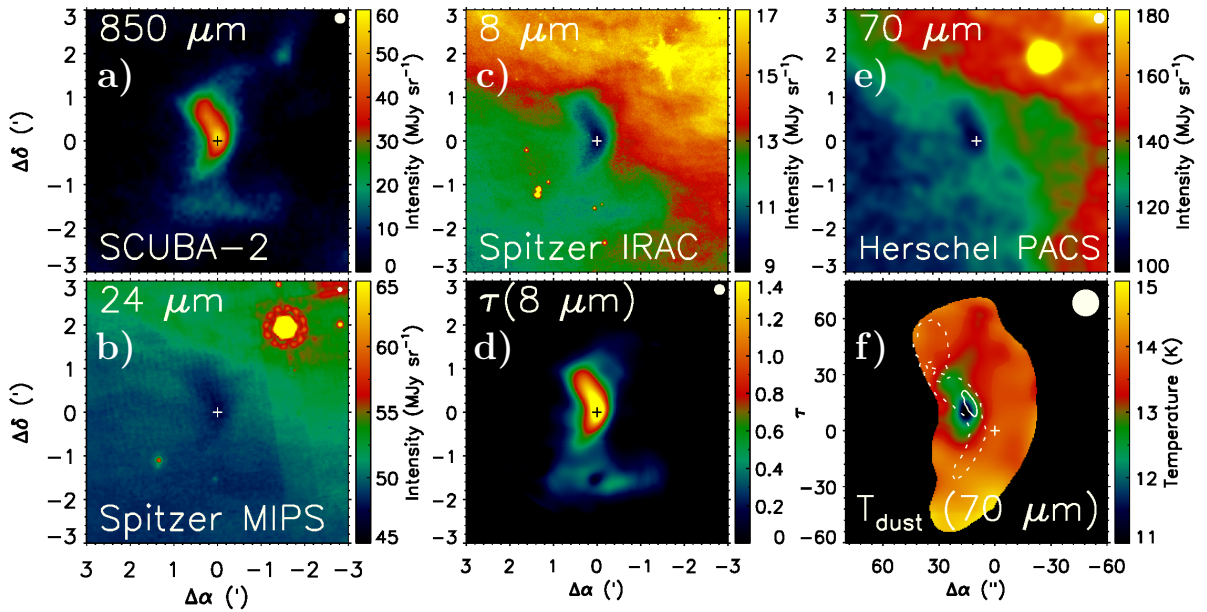


**Figure 5.** Surface brightness maps of H-MM1 at selected mid- to far-infrared wavelengths (panels a to d), and the optical thickness (e) and the dust temperature (f) maps derived from these. The instruments and wavelengths are indicated in panels a) to d). The optical thickness map in panel e),  $\tau^{8\mu\text{m}}$ , is derived from the Spitzer/IRAC map at  $8\mu\text{m}$ . The dust temperature map,  $T_{\text{dust}}$ , in panel f) is derived using Herschel/PACS map at  $70\mu\text{m}$ . Note that in this method,  $T_{\text{dust}}$  can be only derived when  $\tau^{70\mu\text{m}}$  is finite, and the region shown is smaller than in other panels. The maps presented in panels d), e) and f) are smoothed to the angular resolution of the SCUBA map in panel a) ( $14''$ ). The maps in panels b) and c) are shown at the original resolutions,  $6''$  and  $2''$ , respectively. The angular resolution is indicated with a filled circle in the top right. The region of bright  $\text{CH}_3\text{OH}$  emission is outlined in panel f). The plus sign indicates the position of the column density maximum.

in the core region is shown in the bottom right panel of Figure 5. For the  $T_d$  calculation, the  $8\mu\text{m}$  and  $70\mu\text{m}$  maps were smoothed to the  $14''$  resolution of the SCUBA-2 map.

This map indicates that the dust temperature minimum is shifted east from the column density maximum, and is nearly coincident with the  $\text{CH}_3\text{OH}$  maximum. We tested this result by constructing a core model resembling H-MM1. Here it was assumed that the line-of-sight density distribution has the same shape as the  $\tau^{850\mu\text{m}}$  profile along horizontal cuts across the core. The core was illuminated by an isotropic radiation field plus a point source located on its western side. The dust opacity model was the same as used above. The calculations were done using the dust continuum radiative transfer program described in Juvola (2019). The strengths of the isotropic component and the point source were adjusted until the  $850\mu\text{m}$  and  $70\mu\text{m}$  surface brightness maps agreed with the observations. The dust temperature distribution derived from the simulated  $70\mu\text{m}$  map in the same manner as described above shows a similar shift of the minimum as seen in Figure 5f. In the “true”, three-dimensional distribution, the dust temperature minimum is shifted to the same direction, but lies a little closer to the density peak. This experiment shows that dust temperatures derived from the  $70\mu\text{m}$  surface brightness temperature map can correctly reflect, although exaggerating slightly, the displacement of the dust temperature minimum from the density maximum (and the  $850\mu\text{m}$  peak) caused by anisotropic illumination.

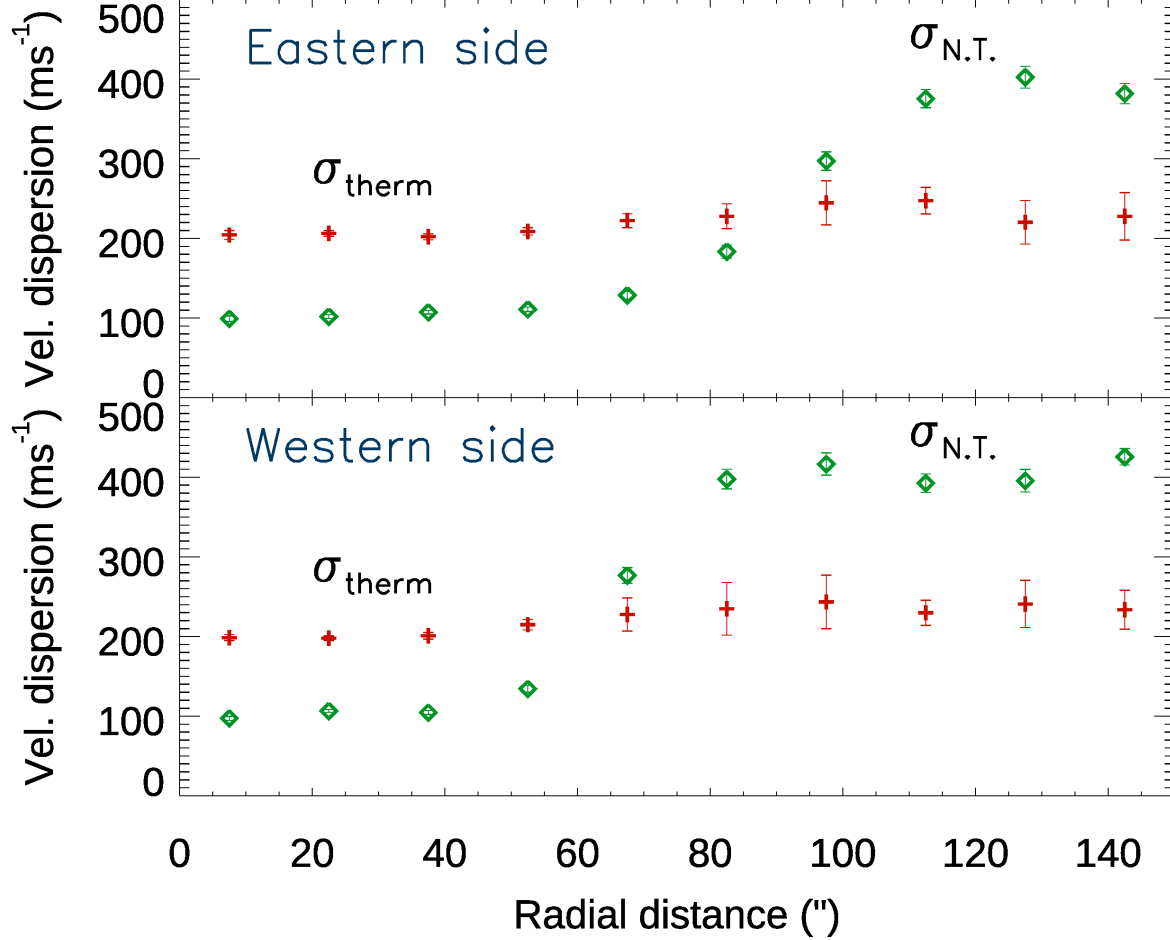


**Figure 6.** Thermal and non-thermal velocity dispersions as functions of the radial distance from the center on the eastern and western sides of H-MM1

### C. VELOCITY DISPERSION PROFILES

Thermal and non-thermal velocity dispersion profiles on the eastern and western sides of the core were calculated using  $\text{NH}_3(1, 1)$  and  $(2, 2)$  inversion line data from the GreenBank Ammonia Survey (GAS; Friesen et al. 2017). The method is described in detail by Auddy et al. (2019). The spectra were first aligned using the Greenbank pipeline-reduced LSR velocity maps, and then averaged in concentric semiannular regions. The stacked  $\text{NH}_3(1, 1)$  and  $(2, 2)$  were analyzed using the standard method described, for example, by Ho & Townes (1983). This analysis gives estimates for the kinetic temperature and total velocity dispersion (along the line of sight). The radial distributions of thermal and non-thermal velocity dispersions were calculated from these data. The results for the two hemispheres of H-MM1 are shown in Figure 6. The non-thermal dispersion is approximately half the sound speed near the center, and reaches a value of  $\sim 400 \text{ ms}^{-1}$ , that is, twice the sound speed far from the center of the core. The transition from subsonic to supersonic regimes occurs, however, closer the center on the western side of the core than the eastern side, where the strongest methanol emission comes from.